

Flux pinning characteristics in cylindrical niobium samples used for superconducting radio frequency cavity fabrication

This article has been downloaded from IOPscience. Please scroll down to see the full text article.

2012 Supercond. Sci. Technol. 25 065014

(<http://iopscience.iop.org/0953-2048/25/6/065014>)

View [the table of contents for this issue](#), or go to the [journal homepage](#) for more

Download details:

IP Address: 129.57.10.46

The article was downloaded on 23/04/2012 at 13:50

Please note that [terms and conditions apply](#).

Flux pinning characteristics in cylindrical niobium samples used for superconducting radio frequency cavity fabrication

Asavari S Dhavale¹, Pashupati Dhakal², Anatolii A Polyanskii³ and Gianluigi Ciovati²

¹ Accelerator and Pulse Power Division, Bhabha Atomic Research Center, Mumbai 400085, India

² Thomas Jefferson National Accelerator Facility, Newport News, VA 23606, USA

³ National High Magnetic Field Laboratory, Florida State University, Tallahassee, FL 32310, USA

E-mail: dhakal@jlab.org

Received 9 December 2011, in final form 7 March 2012

Published 23 April 2012

Online at stacks.iop.org/SUST/25/065014

Abstract

We present the results from DC magnetization and penetration depth measurements of cylindrical bulk large-grain (LG) and fine-grain (FG) niobium samples used for the fabrication of superconducting radio frequency (SRF) cavities. The surface treatment consisted of electropolishing and low-temperature baking as they are typically applied to SRF cavities. The magnetization data are analyzed using a modified critical state model. The critical current density J_c and pinning force F_p are calculated from the magnetization data and their temperature dependence and field dependence are presented. The LG samples have lower critical current density and pinning force density compared to FG samples, favorable to lower flux trapping efficiency. This effect may explain the lower values of residual resistance often observed in LG cavities than FG cavities.

(Some figures may appear in colour only in the online journal)

1. Introduction

Over the past decade, particle accelerators have been relying on superconducting radio frequency (SRF) cavity technology to achieve high accelerating gradients with reduced losses [1]. SRF cavities are mostly made of high-purity (residual resistivity ratio > 300), fine-grain (typical grain size of $\sim 50 \times 50 \mu\text{m}^2$) bulk niobium. Since 2005, large-grain (grain size of few cm^2) Nb discs directly sliced from ingots became a viable option to fabricate SRF cavities with performance comparable to that achieved by standard fine-grain Nb cavities [2]. Large-grain Nb could be, on a large scale, cheaper than fine-grain material. The performance of SRF cavities made of bulk Nb is often limited by a sharp increase of the RF losses starting at peak surface magnetic fields, B_p , greater than about 90 mT. This phenomenon is often referred to as 'high-field Q -slope' or Q -drop [3]. A low-temperature

($\sim 120^\circ\text{C}$ for 12–48 h) baking (LTB) in either argon or ultra-high vacuum (UHV) is often found to be beneficial in reducing the Q -drop. Preliminary theoretical and experimental studies indicate that magnetic vortices pinned near the surface are one among the possible causes for the Q -drop [4]. Magnetic vortices can be introduced in SRF Nb cavities because of the imperfect shielding of the Earth's magnetic field or thermoelectric currents during cavity cool-down across the critical temperature. Magnetic flux can be pinned at material defects, such as grain boundaries, dislocations or clusters of impurities [5, 6].

Flux pinning characteristics of niobium alloys such as NbTi and Nb₃Sn have been studied extensively in the past because of their use in superconducting magnets, where artificial pinning centers are introduced to reduce the dissipation due to the movement of vortices, but fewer

Table 1. Contents in ppm (per weight) of the main interstitial impurities from the different Nb ingots and RRR obtained from the samples' thermal conductivity at 4.2 K.

Sample	Ta (ppm)	H (ppm)	C (ppm)	O (ppm)	N (ppm)	RRR
A	1295	2	<10	21	10	62
B	1310	2	<10	9	3	164
C	603	4	<10	14	9	159
D	644	3	<10	7	7	118
FG	<100	<3	<20	<40	<20	280

reports exist on the pinning properties of single-crystal or polycrystalline high-purity niobium used in SRF applications.

In order to study the pinning properties of Nb, DC magnetization measurements were carried out in the temperature range of 2–8 K on large-grain as well as fine-grain niobium samples treated by electropolishing (EP) and LTB. These treatments are commonly used in the surface preparation of SRF cavities. From measurements of the magnetization curves at different temperatures, the temperature dependence of the field of first flux penetration, H_{fp} , and of the upper critical field, H_{c2} , were obtained. The critical current density as a function of the magnetic flux density was calculated from the irreversible magnetization curve using either the Bean model [7–9] or a modified critical state model as proposed by Matsushita and Yamafuji for superconductors with low Ginzburg–Landau parameter, κ [10]. The field dependence of the pinning force was analyzed using the standard pinning model for type-II superconductors [11–13]. In addition, semi-quantitative measurements of surface pinning characteristics were made at 2 K on the same samples by measuring the change of AC penetration depth during a linear ramp of the DC magnetic field applied parallel to the surface, between zero and 1 T and then back to zero.

2. Experimental setup

2.1. Sample preparation

The large-grain (LG) samples, labeled A to D, were machined from Nb ingots of different purities as shown in table 1, from CBMM, Brazil, while the fine-grain (FG) sample was machined from a solid rod from Wah Chang, USA. The samples used for this study are 6 mm in diameter and 120 mm in length with a 2 mm diameter concentric channel drilled down to about 115 mm. The inner channel was intended as a cooling channel so that the RF properties of the sample's outer surface could be measured by inserting it into a 'pill-box' cavity [14, 15]. This will be part of future studies. Prior to the experiments discussed in this contribution the LG samples were treated according to the following processing steps [16].

- (I) About 180 μm material removal by buffered chemical polishing (BCP) with $\text{HF}:\text{HNO}_3:\text{H}_3\text{PO}_4 = 1:1:1$.
- (II) Heat treatment at 600 °C/10 h in a UHV furnace.
- (III) $\sim 24 \mu\text{m}$ material removal by BCP 1:1:2.

- (IV) Baking in UHV at 100 °C/12, 120 °C/12, 140 °C/12 and 160 °C/12 h. About 10 μm were etched by BCP 1:1:2 after each bake.

The FG sample was treated as follows, prior to the experiments reported in this contribution.

- (I) About 65 μm material removal by BCP with $\text{HF}:\text{HNO}_3:\text{H}_3\text{PO}_4 = 1:1:1$.
- (II) Heat treatment at 800 °C/2 h in a UHV furnace.
- (III) $\sim 140 \mu\text{m}$ material removal by BCP 1:1:1.
- (IV) Heat treatment at 600 °C/10 h in a UHV furnace.
- (V) Post-purification heat treatment of FG sample at 1250 °C for 3 h using Ti as solid state getter.
- (VI) $\sim 100 \mu\text{m}$ material removal by BCP 1:1:1.

After the post-purification heat treatment the typical size of grain boundaries of the FG sample increased from $\sim 50 \mu\text{m}$ to about 1 mm.

Here, we report the results from the measurements carried out on the samples which were subjected to the following surface and heat treatments, after the last step of the initial preparation sequence.

- (I) $\sim 50 \mu\text{m}$ material removal by EP with $\text{HF}:\text{H}_2\text{SO}_4 = 1:10$ acid mixture.
- (II) Baking in UHV at 120 °C for 48 h.

2.2. Magnetization and surface pinning measurement setup

A single-coil magnetometer [17] was built at Jefferson Laboratory to measure the DC magnetization of the hollow cylindrical Nb samples. Two heaters are clamped at the sample ends (distance ~ 70 mm) and two Cernox temperature sensors are also clamped in between (distance ~ 34 mm). A pick-up coil (~ 150 turns, length ~ 30 mm, and 0.28 mm diameter copper wire) is inserted in the center of the sample as shown in figure 1. The sample is clamped on a flanged copper block. The sample assembly is inserted in a copper tube that has a stainless steel Conflat flange brazed on one end and a copper flange on the other end. Indium wire provides the vacuum sealing between the two copper flanges. The assembly is bolted to a vertical test stand and it is concentric to a custom built superconducting magnet from Cryomagnetics INC that provides an axial magnetic field up to 1 T. The magnetic field homogeneity is 0.01% over the length of the pick-up coil. By making the length of the pick-up coil shorter

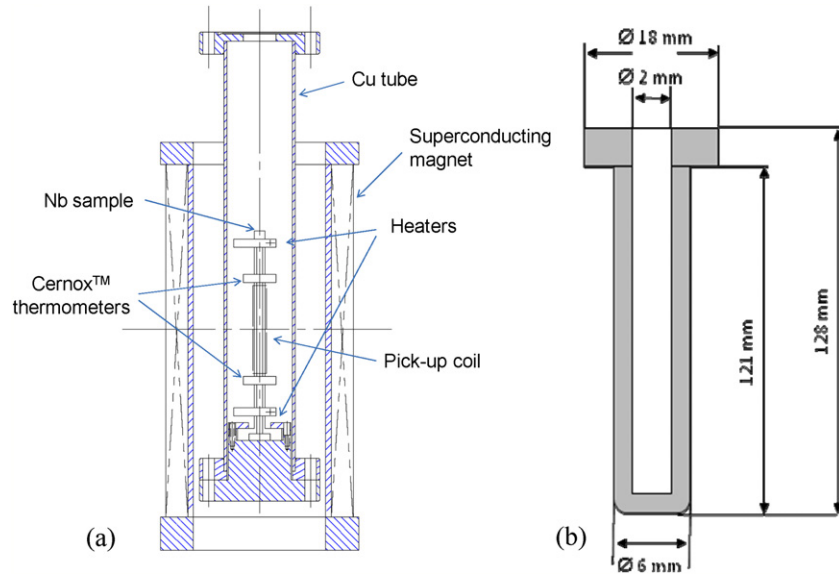


Figure 1. (a) Schematic diagram of the experimental setup and (b) sketch of the sample used.

than the samples' length, edge effects become negligible and greater field homogeneity can be achieved over this shorter length. The inside of the Cu tube is evacuated to a pressure lower than 10^{-4} mbar. The test stand is inserted in a vertical cryostat which is filled with liquid helium at 4.3 K. By pumping on the He bath, a temperature of 2.0 K is achieved.

The sample is zero field cooled (ZFC) from room temperature to 2 K. The DC magnetization measurement is carried out by linearly ramping up the magnetic field of the magnet from 0 to H_e at a ramp rate of 3.87 mT s^{-1} . The induced voltage in the pick-up coil is recorded with a nanovoltmeter (model 2182, Keithley). The single-coil measurement depends critically on the regularity of the field sweeping. For this purpose a computer controlled magnet power supply programmer (model 410, American Magnetics) was used. The magnetization, M , as a function of the applied field, H_e , is calculated by using the following equation [17]:

$$M(H_e) = \left(\frac{-1}{1 - N_d} \right) \int_0^{H_e} \frac{V(H') - V_n}{V_s - V_n} dH' \quad (1)$$

where V_s and V_n indicate the voltages in the superconducting and the normal conducting state, respectively, and N_d is the demagnetization factor (~ 0.001) [18].

The measurements are carried out at various temperatures from 2 to 8 K. The temperature of the sample is changed by using the top and bottom heaters. The temperature over the sample length was monitored using calibrated Cernox temperature sensors. The power to the heaters was controlled by the proportional-integral-differential control loop of a temperature controller (model 332, Lakeshore) to maintain the temperature of the sample within a range of ± 0.1 K about the set point, T_{set} . After each magnetization measurement, the sample was warmed above the transition temperature and slowly cooled down to a new temperature T_{set} in zero field.

By connecting the leads of the pick-up coil to a 30 nF capacitor outside the cryostat as part of an LC oscillator

circuit, it is possible to measure the change in resonant frequency, Δf , as a function of the applied DC magnetic field cycled between zero and 1 T and then back to zero. The change in resonant frequency is proportional, through a geometric constant, to the change in penetration depth [19]. These measurements have been repeated at different temperatures, between 2 and 8 K, and the samples are thermally cycled through T_c , in zero applied fields, after each measurement. The frequency of the oscillator at $H_e = 0$ is ~ 270 kHz, which corresponds to a sampling depth of about $30 \mu\text{m}$ from the surface. The amplitude of the AC magnetic field produced by the coil is about $1.7 \mu\text{T}$. The same oscillator circuit is used to measure the critical temperature of the sample by measuring the frequency change while slowly warming up the samples from 4.3 to 10 K, in zero applied field.

3. Experimental results

3.1. DC magnetization and penetration depth

Figure 2 shows the results of the magnetization measurements carried out on samples D and FG at different temperatures after EP. The observed irreversibility in magnetization is consistent with the flux-line pinning of type-II superconductors. However, the irreversibility was also observed in the absence of bulk pinning [20]. No significant dependence of the $M(H_e)$ curves on the magnetic field ramp rate, between 1.29 and 3.87 mT s^{-1} , was found. Although not shown here, similar results are found for the other samples in these field and temperature ranges. As shown in figure 2(b), the magnetization curves of the FG sample show an unusual curvature in the mixed state, which might be related to the nature of flux pinning. In the case of the FG sample, flux jump was observed at the magnetic field ~ 0.3 T at 2 K, which is believed to be due to the sudden redistribution of vortices

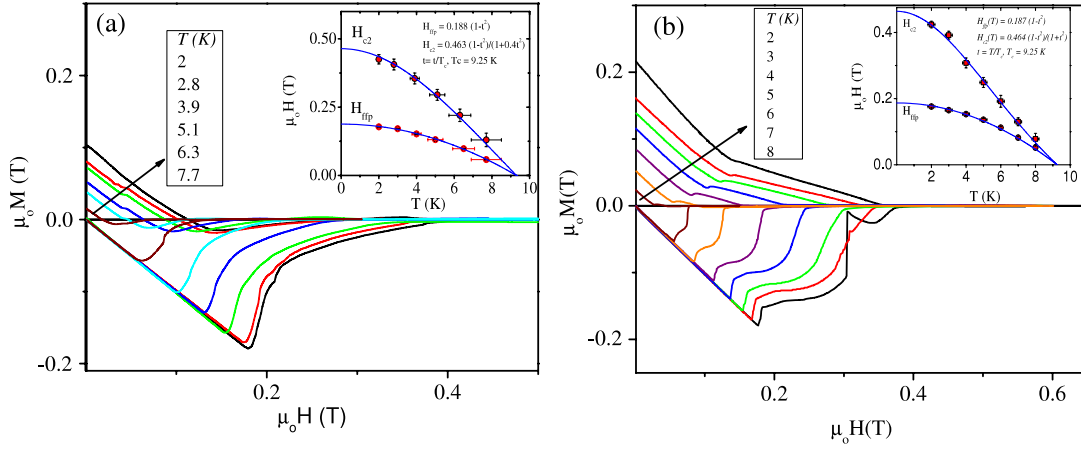


Figure 2. Magnetization curves of samples (a) D and (b) FG at different temperatures after EP. The insets show the temperature dependence of critical fields. The solid lines are calculated using (2)–(4).

Table 2. Critical field values at 0 K obtained by fitting the experimental data. The T_c in the table was measured using the *LC* oscillator circuit.

Sample	EP			EP + LTB (120 °C for 48 h)		
	$\mu_0 H_{ffp}(0)$ (T)	$\mu_0 H_{c2}(0)$ (T)	T_c (K)	$\mu_0 H_{ffp}(0)$ (T)	$\mu_0 H_{c2}(0)$ (T)	T_c (K)
A	0.187 ± 0.005	0.464 ± 0.025	9.25 ± 0.01	0.190 ± 0.007	0.478 ± 0.012	9.22 ± 0.02
B	0.183 ± 0.004	0.442 ± 0.015	9.12 ± 0.02	0.185 ± 0.004	0.468 ± 0.035	9.26 ± 0.02
C	0.194 ± 0.005	0.479 ± 0.014	9.21 ± 0.02	0.193 ± 0.011	0.470 ± 0.023	9.24 ± 0.01
D	0.188 ± 0.005	0.463 ± 0.017	9.21 ± 0.03	0.190 ± 0.009	0.460 ± 0.017	9.24 ± 0.02
FG	0.187 ± 0.003	0.464 ± 0.012	9.34 ± 0.04	0.191 ± 0.01	0.472 ± 0.013	9.27 ± 0.03

caused by thermo-magnetic instabilities [21]. However, the flux jump was not present at higher temperatures. by [26]

The H_{ffp} (H_{c1} , for reversible magnetization) is extracted as the value of the applied field at which the magnetization curve deviates from perfect diamagnetism, i.e., the position at which the magnetization curves deviate from the straight line as the external magnetic field is ramped up from zero to H_c [22]. The temperature dependence of the H_{ffp} and upper critical field H_{c2} (extracted from the criteria $M(H_{c2}) \sim 0$, or the crossover from diamagnetic to paramagnetic state) is plotted as shown in insets of figure 2 for both samples D and FG, subjected to EP surface treatment. For all samples, the $H_{ffp}(T)$ data are fitted well by the following empirical relation:

$$H_{ffp}(T) = H_{ffp}(0)(1 - t^2), \quad (2)$$

where $t = T/T_c$. According to the two-fluid model, the temperature dependence of H_{c2} is given by [23]

$$H_{c2}(T) = H_{c2}(0) \frac{(1 - t^2)}{(1 + t^2)}, \quad (3)$$

but discrepancies between the behavior predicted by this model and experimental data for niobium have been reported in the past [24]. Numerical calculation of the temperature dependence of H_{c2} , based on the solution of the linearized Gor'kov equations, was carried out by Helfand and Werthamer [25]. An approximate analytical formula which deviates by less than 5% from the numerical solution is given

$$H_{c2}(T) = H_{c2}(0) \frac{(1 - t^2)}{(1 + 0.4t^2)}. \quad (4)$$

The $H_{c2}(T)$ data for the FG sample are fitted well by equation (3), whereas the data for the LG samples are better described by (4). The values of $H_{ffp}(T)$ and $H_{c2}(T)$ obtained from magnetization data and curve fits are shown as an inset in figure 2 for samples D and FG. Table 2 summarizes the critical field values at 0 K obtained by fitting experimental data with (2)–(4) for all samples, where $T_c = 9.25$ K is taken for all samples. The estimated value of H_{ffp} is comparable with the values of H_{c1} for high-purity niobium [24, 27]. Also, the estimated H_{c2} values are comparable to the recently reported values for niobium after BCP surface treatments [28]. These experimental results show little or no influence from LTB on the bulk superconducting properties.

Figure 3 shows the change in resonant frequency of the *LC* oscillator as a function of external applied magnetic field at different temperatures for samples C and FG, which is proportional to the change in penetration depth. This will allow us to determine the surface H_{ffp} , H_{c2} and H_{c3} . When the external magnetic field is ramped up, no flux is penetrating and therefore there is no change in the oscillator's resonant frequency. Once the external field reaches H_{ffp} , the flux starts to penetrate and the penetration depth increases gradually. The penetration depth above H_{ffp} depends on the surface barrier (shielding current) as well as the surface pinning. At H_{c2} , the bulk sample becomes stable in its normal state, whereas

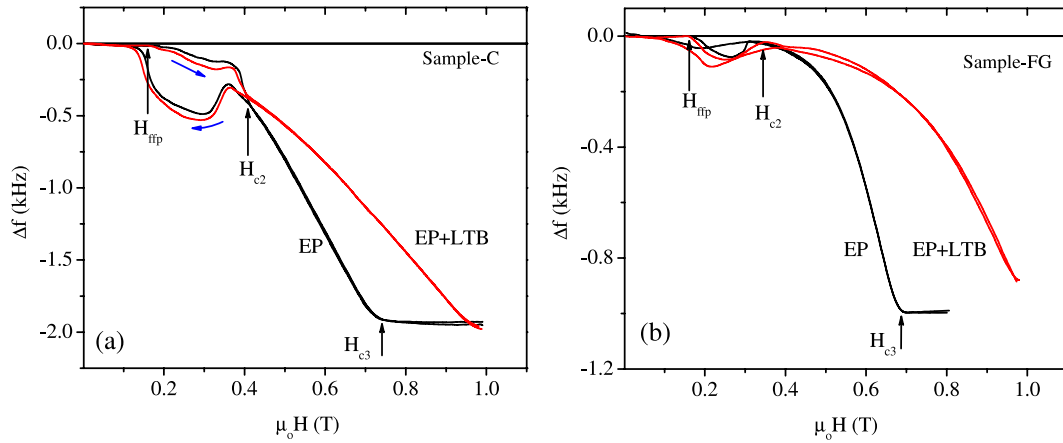


Figure 3. Frequency change as a function of the applied DC magnetic field measured at 2 K after different surface and heat treatments for sample C (a) and sample FG (b). The arrows on the plots indicate the positions of the surface fields H_{ffp} , H_{c2} , and H_{c3} .

Table 3. Critical field values measured within a $\sim 30 \mu\text{m}$ depth from the surface for all samples after EP and EP followed by LTB (120°C for 48 h) at 2 K.

Samples	EP			EP + LTB (120°C for 48 h)		
	$\mu_0 H_{ffp}$ (T)	$\mu_0 H_{c2}$ (T)	$\mu_0 H_{c3}$ (T)	$\mu_0 H_{ffp}$ (T)	$\mu_0 H_{c2}$ (T)	$\mu_0 H_{c3}$ (T)
A	0.178 ± 0.010	0.384 ± 0.010	0.736 ± 0.015	0.173 ± 0.007	0.373 ± 0.011	0.766 ± 0.012
B	0.170 ± 0.006	0.336 ± 0.007	0.705 ± 0.012	0.173 ± 0.007	0.365 ± 0.010	>1
C	0.160 ± 0.008	0.393 ± 0.006	0.753 ± 0.010	0.165 ± 0.010	0.387 ± 0.009	~ 1
D	0.165 ± 0.007	0.345 ± 0.006	0.710 ± 0.013	0.166 ± 0.006	0.347 ± 0.009	0.745 ± 0.012
FG	0.168 ± 0.010	0.358 ± 0.009	0.689 ± 0.015	0.171 ± 0.010	0.362 ± 0.008	>1

the surface superconductivity still exists up to H_{c3} [29]. With decreasing field, the penetration depth is reversible down to H_{c2} and the irreversibility observed below H_{c2} depends on the surface treatment. The larger the irreversibility near H_{ffp} , the stronger the surface barrier. The irreversibility is also expected due to fluxoids which are not in equilibrium with the external magnetic field because of surface pinning caused, for example, by NbO precipitates [30]. Another possible cause of the irreversibility between H_{ffp} and H_{c2} is the slight inhomogeneity of the order parameter, caused by the combination of the induced and diamagnetic screening currents, which is different in increasing and decreasing fields [31]. Table 3 summarizes the surface critical field values within $\sim 30 \mu\text{m}$ depth from the surface for all samples after EP and EP followed by LTB at 2 K. As shown, the surface critical field H_{c3} (or the ratio H_{c3}/H_{c2}) increases due to the LTB. After EP, the ratio H_{c3}/H_{c2} at 2 K is ~ 1.98 , which is in good agreement with the value of 1.93 calculated by Hu and Korenman in the clean limit [32] by extending the result from Saint James and de Gennes near T_c to the region $T \sim 0$ using Gor'kov's theory. The ratio H_{c3}/H_{c2} is increased to even larger values by the LTB and this was explained by the reduction of the electron mean free path due to diffusion of impurities during LTB [28].

3.2. Magneto-optical measurements on FG samples

In order to further understand the unusual curvature in the magnetization measurement of the fine-grain sample

in the mixed state, six 2.5 mm thick samples were cut from the center portion of the rod by wire electro-discharge machining to observe the pattern of flux penetration using the magneto-optical (MO) technique [33]. After cutting, the samples were etched for 2 min by BCP 1:1:2, removing about $6 \mu\text{m}$ of material. The samples have a 'doughnut' shape with an estimated demagnetization factor of about 0.51. The pattern of flux penetration was measured by MO for two out of the six samples. One sample, labeled No 3, showed fairly uniform flux penetration and remnant field as the external magnetic field was cycled between zero and 0.120 T and back to zero, at a temperature of 5.4 K. The other sample, labeled No 5, showed non-uniform flux penetration and remnant field distribution as the applied magnetic field was cycled above H_{ffp} and back to zero at different temperatures, between 6 and 8 K. Figure 4 shows the optical image of the top surface of sample No 5 and the corresponding MO image at 6 K, 0.124 T, indicating a non-uniform flux penetration, with some preferential flux entry through some of the grain boundaries. Evidence for preferential flux penetration at grain boundaries has been reported in a detailed study of high-purity Nb samples by MO imaging [34], and the results showed, in particular, that the occurrence of this phenomenon strongly depends on the orientation between the applied field and the grain boundary plane. The H_{ffp} values measured by MO at different temperatures in the range 6.5–9 K are consistent with those obtained for the full rod with the single-coil magnetometer. The MO results suggest that the unusual curvature in the mixed state in the $M(H)$ plot of figure 2(b)

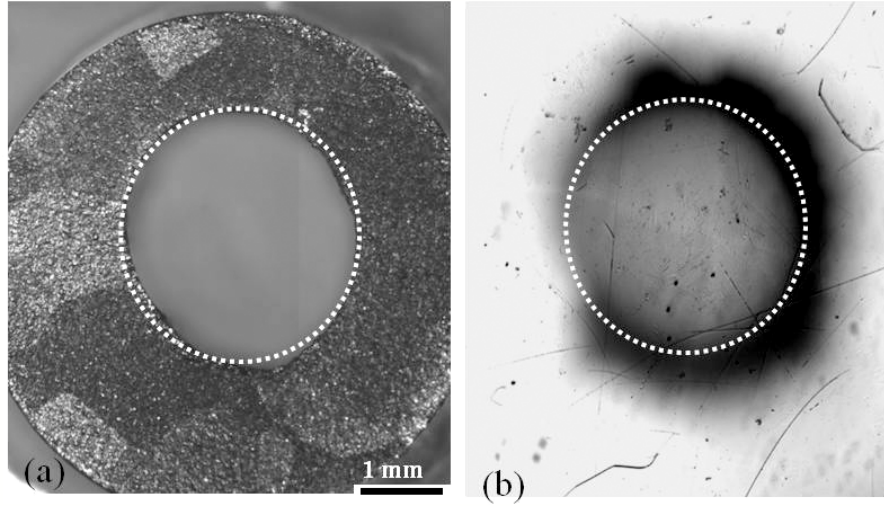


Figure 4. Optical image (a) of the cross-section of sample No 5 cut from the FG hollow rod sample and MO image (b) after zero field cooling of the same sample at 6 K and 0.124 T. The dark areas in (b) indicate flux-free regions of the sample.

could be due to the inhomogeneous flux distribution in the volume sampled by the coil.

4. Calculation of critical current density and pinning force

4.1. Critical state models

Bean's model is one of the most widely used critical state models to describe the field and current distribution in a superconductor [7–9]. The critical state describes a current distribution throughout the superconductor determined by the effectiveness of material inhomogeneities in pinning the flux distribution against Lorentz forces [35]. This allowed us to determine the field dependent critical current density $J_c(B)$ in terms of the measured values of magnetization, under the assumption of full flux penetration and uniform flux distribution, as

$$J_c(B) = \frac{3}{2} \Delta M(B) \left(\frac{R_{\text{out}}^2 - R_{\text{in}}^2}{R_{\text{out}}^3 - R_{\text{in}}^3} \right) \quad (5)$$

where $\Delta M(B)$ is the hysteresis when the externally applied field is increased or decreased about B/μ_0 . Here, R_{out} is the outer radius and R_{in} is the inner radius of the sample. In the critical state of the superconductor the current density is equal to the critical value J_c and the pinning force exactly balances the Lorentz force. Therefore, the pinning force density F_p can be calculated as

$$F_p(B) = J_c(B)B. \quad (6)$$

Even though the Bean model successfully explained the critical state of the high κ type-II superconductor, it deviates for the low κ and weakly pinned superconductors where the diamagnetic contribution to the critical state is significant. Much work has been done to understand the origin of the experimentally observed irreversible magnetization in low κ type-II superconductors [36–40]. In all those models, several

assumptions and empirical parameters were used to obtain a good fit of the experimental data, but there is no clear consensus on which one provides the most accurate physical description of the magnetic properties of low κ type-II superconductors. For this study, we considered the modified critical state model proposed by Matsushita and Yamafuji. The model is described in detail in [10, 13]. The magnetic field and flux density profiles in a cylindrical sample, $R_{\text{in}} \leq r \leq R_{\text{out}}$, are calculated numerically and the magnetization is obtained as

$$M = -\mu_0 H_e \pm \frac{B_{c2}^2}{\alpha(R_{\text{out}} - R_{\text{in}})} \times \int_{H(r=R_{\text{in}})}^{H_e} \left[\frac{B(H)}{B_{c2}} \right]^{2-\gamma} \left[1 - \frac{B(H)}{B_{c2}} \right]^{-\delta} dH \quad (7)$$

where the positive sign is for increasing external field and the negative sign is for decreasing field. α , γ and δ are fit parameters resulting from the widely used empirical law that was assumed for the pinning force density [41]:

$$F_p(B) = \alpha \left(\frac{B}{B_{c2}} \right)^\gamma \left(1 - \frac{B}{B_{c2}} \right)^\delta. \quad (8)$$

For decreasing external field, H_e , the following dependence $H(r)$ is proposed in the model:

$$H(R) = \frac{a}{b} (1 - e^{-bR}) \quad \text{for } 0 \leq H_e \leq H_{c1} \quad (9)$$

with a and b being two additional fit parameters, $R = r + r_0$, where r_0 is chosen as $H = 0$ at $R = 0$. The parameter a corresponds to the critical current density at $H_e = 0$.

The experimental data for the magnetization as a function of reduced magnetic field (H/H_{c2}) for sample B after EP and LTB treatment are shown in figure 5. The symbols in figure 5 are obtained from a calculation of the magnetization using (7) with the parameters listed in table 4, showing an excellent agreement with experimental data. The data for all LG samples could be fitted well with (7). The modified critical

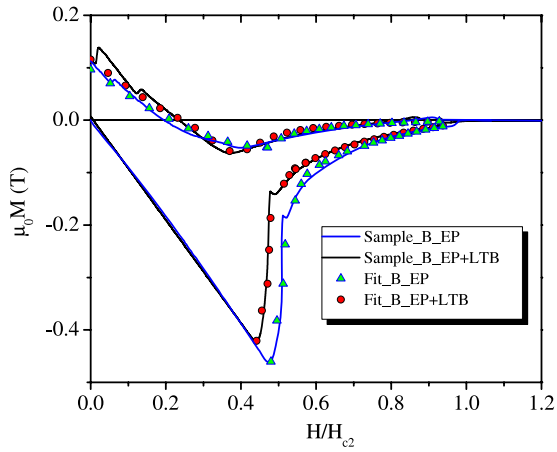


Figure 5. Magnetization as a function of reduced applied field (H/H_{c2}) for sample B after EP and LTB treatments at 2 K. The solid lines are the experimental data whereas the points are the results of numerical calculations using the modified critical state model with the parameters given in table 4.

Table 4. The parameters used to fit the experimental magnetization curves using the modified critical state model of Matsushita and Yamafuji [10].

Fitting parameters	Sample B		Sample FG	
	EP	EP + LTB	EP	EP + LTB
α (N m^{-3})	8.38×10^6	8.08×10^6	2.38×10^7	2.13×10^7
γ	1	1	0.5	0.5
δ	1.25	1.25	1.25	1.25
β	0.08	0.08	0.05	0.05
a (A m^{-2})	1.29×10^8	1.37×10^8	3.5×10^8	3.37×10^8
b (m^{-1})	4.26×10^2	4.31×10^2	5.13×10^2	5.06×10^2

state model cannot provide a good fit of the magnetization curve for the FG sample in increasing field, between H_{fp} and H_{c2} , due to the unusual curvature of $M(H)$ in the mixed state which we attribute to a highly non-uniform flux distribution in the sample's volume, because of preferential flux entry along the grain boundaries.

4.2. Critical current density and pinning force

Figure 6 shows a plot of the critical current density at 2 K as a function of reduced magnetic flux density ($b = B/B_{c2}$) for sample D after EP, calculated using Bean's model (equation (5)) from the experimental data. Using the modified critical state model described above, it is also possible to calculate the critical current density from (6) and (8), as shown in figure 6. The critical current density calculated using Bean's critical state model and the modified critical state model of Matsushita and Yamafuji are in good agreement at high magnetic flux density; however, a large deviation is observed at low field ($b \sim 0.13$). This is consistent with previous studies showing that Bean's model underestimates J_c at low magnetic flux densities even for high κ superconductors, compared to other critical state models which better describe the magnetization data [42, 43].

4.3. Flux pinning mechanism

The pinning force depends on the temperature, the applied magnetic field and the microstructure of the sample. Any dislocation networks, grain boundaries or surface precipitation with sizes of the order of the coherence length (about 40 nm in Nb) can act as a pinning center. These pinning centers are randomly distributed within the sample and are capable of pinning one or multiple vortices at a particular site. In view of this scenario, it is not possible to give an exact mathematical expression for the basic pinning force involved, but one can analyze the scaling of the pinning force with various parameters.

In a simple case where vortices are randomly distributed and the applied magnetic field is not very large (near H_{fp}), each pinning site can be considered as independent and the total pinning force is just the summation due to all the pinning sites. Considering N_p as the number of pinning sites in a unit volume and f_p as the elementary pinning force involved, the total pinning force density has a simple dependence

$$F_p \propto N_p f_p. \quad (10)$$

As the magnetic field is increased, the spacing between the vortices is reduced and therefore an attractive or repulsive interaction between vortices results in a pinning force that is less than the mere summation of force due to individual vortices. In short, the average superconducting order parameter and hence the average magnetic induction is changed with variation in the applied magnetic field. Thus, the experimental curves show a maximum at a particular value of the reduced magnetic flux density, b . An empirical scaling law of the pinning force per unit volume, F_p , is given by [35]

$$F_p \propto H_{c2}^m f(b) \approx H_{c2}^m b^\gamma (1-b)^\delta. \quad (11)$$

In order to understand the intrinsic pinning mechanism of the system, the normalized pinning force density $F_p/F_p(\text{max})$, calculated from (6), was plotted against the reduced magnetic flux density b as shown in figure 7 for samples D and FG after EP. The critical current density from Bean's model was used in (6). As shown in figure 7, $F_p/F_p(\text{max})$ as a function of b follows the same curve at all temperatures, suggesting that the basic pinning force in a sample is unique and depends on the microstructure (grain size). The normalized pinning force has the peak value at a reduced magnetic flux density of 0.34 ± 0.02 for sample D, whereas it is 0.46 ± 0.02 for the FG sample. It was reported that for materials containing a second phase, or grain boundaries, the maximum in normalized pinning force occurs at about 0.33, for dislocation pinning; on the other hand, it can vary between 0.25 and 0.8 depending on the deformation structures [37]. In this case, a large shift of the peak in normalized pinning force to a higher value is observed in the FG sample.

We have also plotted the approximate fit to the normalized pinning force with the function $F_p/F_p(\text{max}) = Ab^\gamma (1-b)^\delta$ with the parameters $A = 5.2$, $\gamma = 0.9$ and $\delta = 1.65$ for sample D, whereas $A = 7.4$, $\gamma = 1.35$ and $\delta = 1.58$ for sample FG. The value of peak reduced magnetic flux density can be calculated to be $b_{\text{peak}} = \gamma/(\gamma+\delta)$, which yields

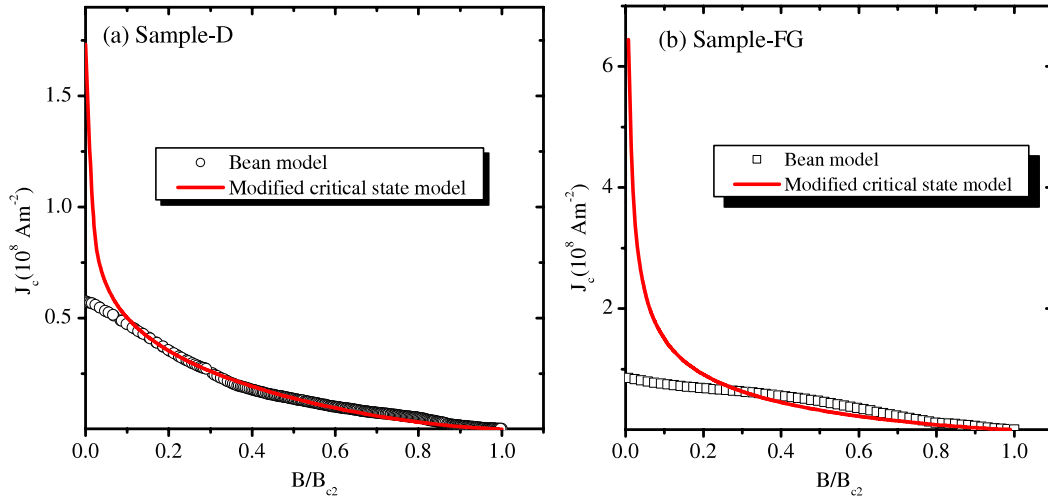


Figure 6. Critical current density as a function of reduced magnetic flux density ($b = B/B_{c2}$) at 2 K for (a) sample D and (b) sample FG after EP surface treatment. The critical current density is calculated from magnetization data using Bean's model and the modified critical state model described in the text.

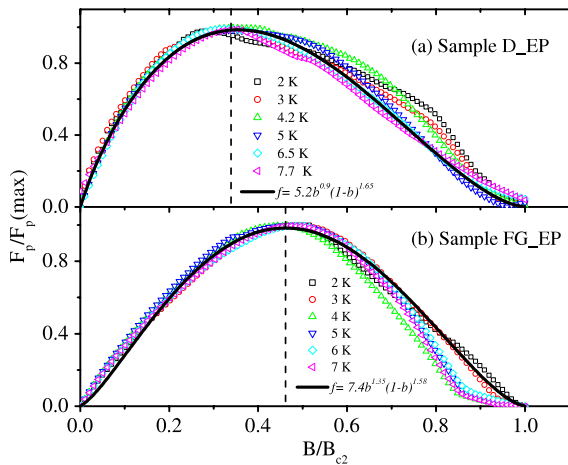


Figure 7. Normalized pinning force versus the reduced magnetic flux density $b = B/B_{c2}$ at different temperatures for samples D (a) and FG (b) after EP surface treatments. The solid line is an approximate fit to the experimental data.

$b_{\text{peak}} = 0.36$ for sample D and $b_{\text{peak}} = 0.46$ for sample FG. This scaling expression fits well the experimental data up to b_{peak} ; however, some deviations are visible closer to B_{c2} .

The temperature dependence of F_p is defined by the first term in (11) while terms containing reduced magnetic flux density define the basic pinning force. A plot of the maximum pinning force $F_p(\text{max})$ at different temperatures and the corresponding upper critical field $H_{c2}(T)$ is shown in figure 8. The slope of the straight line fit gives the index m and hence the dependence of F_p on $H_{c2}(T)$. In all the LG samples we studied $m \sim 1.5 \pm 0.01$, and in the case of FG $m = 1.82 \pm 0.02$.

5. Discussion

The results on the critical current density showed no correlation with the RRR of the samples and therefore with

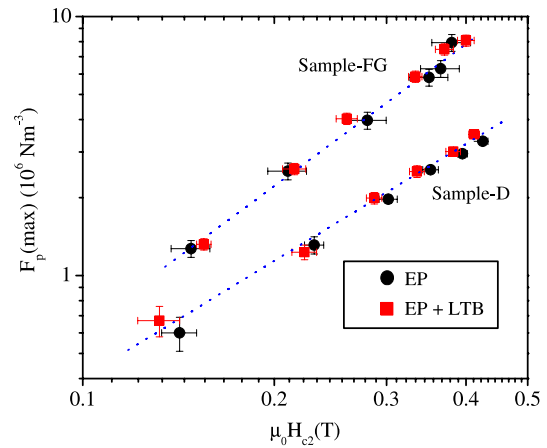


Figure 8. Scaling of the maximum pinning force with the upper critical field for sample D after EP and LTB. The dotted line is the result of the fit $F_p(\text{max}) \sim H_{c2}^m$, yielding $m = 1.50 \pm 0.01$ for sample D and $m = 1.82 \pm 0.02$ for sample FG.

the bulk impurity concentrations. Measurements of the depth profile of the critical current density on low-purity (RRR ~ 40) Nb samples indicated J_c values at 4.2 K up to about $5 \times 10^{10} \text{ A m}^{-2}$ at the surface, leveling off to less than about $2 \times 10^7 \text{ A m}^{-2}$ at a depth of about $10 \mu\text{m}$ [44]. Similar results were obtained on single-crystal samples of the same purity. Oxygen depth profiles calculated from values of H_{c2} measured at different depths indicated oxygen concentrations above 400 at. ppm within a $30 \mu\text{m}$ depth from the surface. From these results, it was inferred that material inhomogeneities, such as oxygen and hydrogen precipitates, dominated the pinning mechanism. For the higher-purity Nb which is now available for SRF cavity fabrication, the concentration of impurities has been significantly reduced and the influence of grain boundary on pinning properties is more evident, as shown by the large-grain and fine-grain samples measured in this study. Impurity depth profiling by secondary ion mass

spectrometry showed O, N and C levels below 180 at. ppm [45]. On the other hand, hydrogen concentrations of several tens of atomic per cent have been measured near the surface [46], as hydrogen is readily absorbed into Nb during chemical treatments.

Penetration depth measurements as a function of an applied external magnetic field showed, after LTB, not only an increase of H_{c3} but also a broadening of the transition to H_{c3} . Such broadening can occur due to surface roughness or material inhomogeneities. Since baking at 120 °C does not affect the surface roughness, the measurement results suggest an increase of surface inhomogeneities. The increase of the ratio H_{c3}/H_{c2} after baking was explained by the presence of an impurity layer of thickness smaller than the coherence length [28]. Oxygen diffusion within a 50 nm depth from the surface had been proposed as a possible explanation of the baking effect [47], but experiments trying to test the validity of the model showed contradicting results (see for example the review in [45]).

In relation to the application to SRF cavity fabrication, the results presented in this contribution indicate that large-grain Nb would be less effective in pinning magnetic flux during the cavity cool-down, compared to fine-grain Nb, because of the lower J_c . This would result in reduced RF losses (higher Q_0 -value) for large-grain cavities. Results on direct measurements of trapped flux in fine-grain and large-grain Nb samples were recently reported [48] and showed a lower trapping efficiency in large-grain Nb, consistent with our conclusion. Furthermore, comparison of several cavities' RF test results at DESY, Germany [49], and Jefferson Lab [50] indicate lower residual resistance and higher Q_0 -values in large-grain compared to fine-grain cavities which underwent similar surface treatments.

6. Conclusions

DC magnetization measurements carried out on large-grain Nb samples of different purities and one fine-grain Nb sample of high purity at various temperatures allowed us to obtain the field and temperature dependence of the critical current density and pinning force on such samples. Using the modified critical state model by Matsushita and Yamafuji, the irreversible magnetization was calculated, showing good agreement with the experimental data. The calculated J_c and F_p of large-grain samples (A–D) are lower than the FG, as expected because of the fewer grain boundaries. Even though the LG samples have different RRR values, the magnetic properties of these large-grain samples do not depend on the bulk impurity concentrations. Because of the lower J_c -value, it is expected that large-grain niobium would have lower pinning efficiency than fine-grain Nb. This should result in lower RF losses and therefore higher Q_0 -values for large-grain cavities. Recent results on cavities and samples confirmed these findings. The improvement of Q_0 at 2 K and accelerating gradients of about 20 MV m⁻¹ is important in order to reduce the cryogenic losses in superconducting continuous wave accelerators for a variety of applications.

Acknowledgments

The authors would like to acknowledge Drs G R Myneni, K C Mittal, and Professor A V Gurevich for several interesting discussions. The authors would also like to acknowledge P Kushnick and M Morrone at Jefferson Lab for technical support.

This paper has been authored by Jefferson Science Associates, LLC, under US DOE contract No DE-AC05-06OR23177. The US Government retains a non-exclusive, paid-up, irrevocable, world-wide license to publish or reproduce this paper for US Government purposes.

References

- [1] Padamsee H 2008 *RF Superconductivity Science, Technology and Applications* (Weinheim: Wiley–VCH)
- [2] Kneisel P, Myneni G R, Ciovati G, Sekutowicz J and Carneiro T 2006 Development of large grain/single crystal niobium cavity technology at Jefferson Lab *Proc. Int. Niobium Workshop on Single Crystal—Large Grain Technology (Araxá) (AIP Conf. Proc. vol 927)* ed G Myneni *et al* (Melville: American Institute of Physics) pp 84–97
- [3] Kako E *et al* 1997 Cavity performances in the 1.3 GHz saclay/KEK Nb cavities *Proc. 8th Workshop on RF Superconductivity (Abano Terme, Oct. 1997)* ed V Palmieri, pp 491–502 INFN Report LNL-INFN 133/98
- [4] Gurevich A and Ciovati G 2008 *Phys. Rev. B* **77** 104501
- [5] Ciovati G and Gurevich A 2008 *Phys. Rev. Spec. Top.—Accelerators Beams* **11** 122001
- [6] Gurevich A 2006 *Physica C* **441** 38–43
- [7] Bean C 1962 *Phys. Rev. Lett.* **8** 250–3
- [8] Bean C 1964 *Rev. Mod. Phys.* **36** 31–9
- [9] Kim Y B, Hempstead C F and Strnad A R 1962 *Phys. Rev. Lett.* **9** 306–9
- [10] Matsushita T and Yamafuji K 1979 *J. Phys. Soc. Japan* **46** 764–71
- [11] Dew-Hughes D 1974 *Phil. Mag.* **30** 293
- [12] Brandt E H 1995 *Rep. Prog. Phys.* **58** 1465–594
- [13] Matsushita T 2007 *Flux Pinning in Superconductors* (Berlin: Springer) pp 66–76
- [14] Ciovati G, Kneisel P, Myneni G R, Morrone M, Bundy R, Clemens B, Elliott T, Slack G, Turlington L and Mondal J 2007 A coaxial TE₀₁₁ cavity and a system to measure DC and RF properties of superconductors *Proc. 13th Workshop on RF Superconductivity (Beijing, Oct. 2007)* ed J K Hao *et al* (Beijing: Peking University) pp 98–102
- [15] Dhakal P, Ciovati G, Kneisel P and Myneni G R 2011 Superconducting DC and RF properties of ingot niobium *Proc. 15th Int. Conf. on RF Superconductivity (Chicago, July 2011)* THPO057, arXiv:1202.0811
- [16] Mondal J, Mittal K C, Ciovati C, Kneisel P and Myneni G R 2009 Characterization of ingot material for SRF cavity production *Proc. 14th Int. Conf. on RF Superconductivity (Berlin, Sept. 2009)* ed M Abo-Bakr *et al* (Berlin: Helmholtz Zentrum Berlin) pp 455–61
- [17] Imfeld N J, Bestgen W and Rinderer L 1985 *J. Low Temp. Phys.* **60** 223–38
- [18] Chen D X, Burg A and Goldfarb R B 1991 *IEEE Trans. Magn.* **27** 3601–19
- [19] Schawlow A L and Devlin G E 1959 *Phys. Rev.* **113** 120–6
- [20] Clem J R, Kerchner H R and Sukela S T 1976 *Phys. Rev. B* **14** 1893–901

- [21] Tinkham M 2004 *Introduction to Superconductivity* 2nd edn (Mineola: Dover)
- [22] Roy S B *et al* 2008 *Supercond. Sci. Technol.* **21** 065002
- [23] Tinkham M 1963 *Phys. Rev.* **129** 2413–22
- [24] Finnemore D K, Stromberg F T and Swenson C A 1966 *Phys. Rev.* **149** 231–43
- [25] Helfand E and Werthamer N R 1966 *Phys. Rev.* **147** 288–94
- [26] Gurevich A 2012 private communication
- [27] Saito K 2003 *Proc. 11th Workshop on RF Superconductivity (Travemünde, Sept. 2003)* ed D Proch (Hamburg: DESY) pp 1–16
- [28] Casalbuoni S, Knabbe E A, Kotzler J, Lilje L, von Sawilski L, Schmuser P and Steffen B 2005 *Nucl. Instrum. Methods Phys. Res. A* **538** 45–64
- [29] de Gennes P G 1966 *Superconductivity of Metals and Alloy* (New York: Benjamin)
- [30] Kneisel P, Stoltz O and Halbritter J 1974 *J. Appl. Phys.* **45** 2296–302
- [31] Park J G 1965 *Phys. Rev. Lett.* **15** 352–5
- [32] Hu C-H and Korenman V 1969 *Phys. Rev.* **185** 672–82
- [33] Lee P J, Polyanskii A A, Gurevich A, Squitieri A A, Larbalestier D C, Bauer P C, Boffo C and Edwards H T 2006 *Physica C* **441** 126–9
- [34] Polyanskii A A, Lee P J, Gurevich A, Zu-Hawn S and Larbalestier D C 2010 Magneto-optical study of high-purity niobium for superconducting RF application *Proc. Int. Symp. on the Superconducting Science and Technology of Ingot Niobium (Newport News, Sept. 2010) (AIP Conf. Proc. vol 1352)* ed G R Myneni *et al* (Melville: American Institute of Physics) pp 186–202
- [35] Fietz W A and Webb W W 1969 *Phys. Rev.* **178** 657–67
- [36] Goedemoed S H, Kes P H, Jacobs F T A and de Klerk D 1967 *Physica* **35** 273
- [37] Campbell A M, Evetts J E and Dew-Hughes D 1968 *Phil. Mag.* **18** 313
- [38] Dew-Hughes D 1971 *Rep. Prog. Phys.* **34** 821–73
- [39] Kes P H, van der Klein C A M and de Klerk D 1973 *J. Low Temp. Phys.* **10** 759–79
- [40] Clem J R 1973 *Low Temp. Phys.* **13** 102–6
- [41] Campbell A M and Evetts J E 1972 *Adv. Phys.* **21** 199
- [42] Douine B, Leveque J and Mezani S 2010 *IEEE Trans. Appl. Supercond.* **20** 82–6
- [43] Chaddah P 1991 *Pramana J. Phys.* **36** 353–92
- [44] Gupta A D, Gey W, Halbritter J, Küpfer H and Yasaitis J A 1976 *J. Appl. Phys.* **47** 2146–53
- [45] Ciovati G, Myneni G, Stevie F, Maheswari P and Griffis D 2010 *Phys. Rev. Spec. Top.—Accelerators Beams* **13** 022002
- [46] Ciovati G 2004 *J. Appl. Phys.* **96** 1591–600
- [47] Ciovati G 2006 *Appl. Phys. Lett.* **89** 022507
- [48] Aull S, Knobloch J and Kugeler O 2011 Study of trapped magnetic flux in superconducting niobium samples *Proc. 15th Int. Conf. on RF Superconductivity (Chicago, July 2011)* THPO006
- [49] Singer W *et al* 2011 Advances in large grain resonators for the European XFEL *Proc. Int. Symp. on the Superconducting Science and Technology of Ingot Niobium (Newport News, Sept. 2010) (AIP Conf. Proc. vol 1352)* ed G R Myneni *et al* (Melville: American Institute of Physics) pp 13–24
- [50] Ciovati G, Kneisel P and Myneni G R 2011 America's overview of superconducting science and technology of ingot niobium *Proc. Int. Symp. on the Superconducting Science and Technology of Ingot Niobium (Newport News, Sept. 2010) (AIP Conf. Proc. vol 1352)* ed G R Myneni *et al* (Melville: American Institute of Physics) pp 25–37